Available online at www.sciencedirect.com
ScienceDirect
Trans. Nonferrous Met. Soc. China 33(2023) 802−815
Transactions of Nonferrous Metals Society of China
www.tnmsc.cn

Effect of deformation degree on microstructure and mechanical properties evolution of TiB_w/Ti60 composites during isothermal forging

Fang-zhou ZHANG, Bo WANG, Qing-hua CAO, Li ZHANG, Hao-yang ZHANG

School of Materials Engineering, Shanghai University of Engineering Science, Shanghai 201600, China

Received 17 November 2021; accepted 4 March 2022

Abstract: In order to investigate the influence of deformation degree on microstructure and mechanical properties during hot compression, TiB whiskers reinforced Ti60 composites were subjected to isothermal forging at 1030 ℃ and strain rate of 1×10^{-2} s^{-1} under 30%, 50%, and 70% deformation degrees. The results showed that with strain increasing, the fraction of high angle grain boundaries (HAGBs) significantly increased to 71.47% at 70% deformation degree, and the texture components of α_s colonies gradually became dominant due to the enhanced recrystallization efficiency. TiB can promote nucleation of recrystallized grains and impede grain growth. After isothermal forging, the mechanical properties of composites at both RT and 600 ℃ were improved, and the specimen compressed at 50% deformation degree showed the best tensile strength and elongation. During tensile tests, the TiB whiskers can bear the load transmitted from surrounding matrix, showing strengthening effect on the material.

Key words: titanium matrix composites; isothermal forging; dynamic recrystallization; texture evolution; mechanical properties

1 Introduction

With the development of aviation industry, more requirements are put forward for new high temperature titanium alloys because of the advantages of lightweight, high temperature stability, and creep resistance, etc [1,2]. The near-α titanium alloys are widely used in the fabrication of jet engine high pressure parts of axial compressors due to the superior performance at elevated temperatures. Compared with IMI834 titanium alloys, Ti60 alloy shows better thermal stability and high temperature oxidation resistance, which can serve at 600 ℃ over a long time. In order to obtain better mechanical properties like higher specific strength, specific modulus and temperature durability [3,4], titanium matrix composites (TMCs) were fabricated by in situ methods of reaction hot pressing (RHP), for the advantages of micro-structure controlling, near net shape processing and the minimal material waste [5]. Researchers found that TiB has many advantages like higher elastic modulus, thermal stability and similar coefficient of thermal expansion with Ti60 matrix, which is a good reinforcement candidate for TMCs. The mechanical properties of materials are primarily determined by the microstructure morphology and texture [6]. It has been widely reported that the titanium microstructure is sensitive to many working parameters like working temperature, strain rate and strain [7], so an appropriate processing parameter and precise control is extremely important during the hot working [8], and the isothermal forging method was applied to further optimizing the process window [9].

LÜ et al [10] obtained refined TiC_p/near-β Ti composite transformed from primary coarse grains of heat treated material after isothermal forging, and the comprehensive tensile properties were

Corresponding author: Bo WANG, Tel: +86-21-67791203, E-mail: wangbo@sues.edu.cn
DOI: 10.1016/S1003-6326(23)66147-3

significantly improved. WANG et al [11] investigated the effect of isothermal forging temperature on the microstructure morphology and mechanical properties of Ti−22Al−25Nb alloy, as working temperature increased from 1040 to 1080 ℃, the morphology showed equiaxial, duplex, and bimodal-size lamellar orthorhombic respectively, which exhibited different tensile strength, creep resistance and ductility performance. Thus, the desired microstructure and mechanical properties can be obtained through well controlled isothermal forging process. Nowadays, the research about TMCs is still limited, especially the influence of deformation degree on the composites during hot compression. Therefore, it is necessary to investigate the microstructure evolution and mechanical properties of TMCs under different working parameters, which has a practical guidance for industrial production.

The purpose of current work was to investigate the influence of deformation degree on the microstructure, texture evolution and mechanical properties of TiB_w/Ti60 composites during two-phase isothermal forging. The in situ synthesis and isothermal forging methods were employed. The surface morphology characterizations were carried out through scanning electron microscopy (SEM) and electron backscattered diffraction (EBSD) technique. The dynamic recrystallization (DRX) and fracture behavior were investigated in detail.

2 Experimental

2.1 Material

The 5.1vol.%TiB_w/Ti60 composite with starting duplex microstructure was used in this study, which was in situ synthesized by reaction hot pressing, and the RHP reaction can be expressed as

$$Ti+TiB_2=2TiB \quad (1)$$

The chemical composition is listed in Table 1. The TiB whiskers were completely synthesized under vacuum (10^{-2} Pa) at 1300 ℃ and the pressure of 25 MPa for 60 min, finally the 5.1vol.%TiB_w/Ti60 composite with a novel network structure was obtained. The average grain size after RHP was ~63.54 μm, and the β transus temperature was ~1070 ℃. According to the characteristic of powder metallurgy, the initial material showed similar morphology and property in all areas and directions. Three cylindrical specimens with a diameter of 22 mm and a height of 15 mm were cut from the as-received billet for the following experiments.

Table 1 Chemical composition of as-received 5.1vol.% TiB_w/Ti60 composite (wt.%)

Al	Sn	Zr	Mo	Si	Nb	Ta	C	B	Ti
5.80	4.00	3.50	0.40	0.40	0.40	0.10	0.06	0.94	Bal.

2.2 Method

The isothermal forging process was performed at 1030 ℃ and strain rate of 1×10^{-2} s^{-1} on the Gleeble−3800 thermal simulator. Thermocouples were welded in the middle surface of the specimens to heat and monitor the temperature. The specimens were heated to the testing temperatures with a heating rate of 10 ℃/s, held for 5 min and compressed with deformation degree of 30%, 50% and 70%, respectively, followed by air cooling. The testing specimens were all cut in the geometric center of the forged materials for optical observation.

The specimens were mechanically polished and etched in the Kroll's reagent (5 mL HF, 10 mL HNO_3, and 85 mL H_2O) for SEM characterization. After SEM observation, the specimens were mechanically polished once again and employed ion polishing (6.5 kV, 8°, 20 min → 5 kV, 6°, 20 min → 3 kV, 4°, 40 min) for EBSD characterization, the scanning step size was 0.7 μm, and the scanning area was 200 μm × 200 μm. The analyses were carried out on TESCAN LYRA3 scanning electron microscope and NordlysMax^3 EBSD Detector. The tensile tests were performed on Zwick/Roell Z100 testing system at a constant strain rate of 1×10^{-3} s^{-1}.

In the scanned EBSD map, the macroscopic coordinate system (Fig. 1) consisted of a forging direction (FD) parallel to the compression axis and

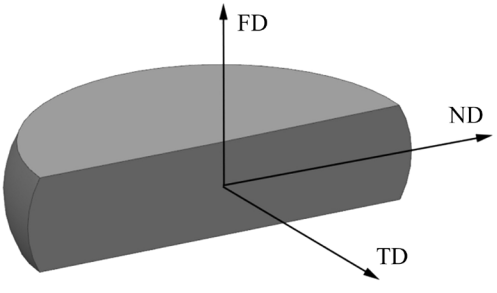

Fig. 1 Coordinate system of material

two mutually perpendicular normal direction (ND) and transverse direction (TD), which were arbitrarily chose [12]. The inverse pole figure (IPF) maps were acquired with respect to the forging direction, in which the misorientation angles larger than 15° were defined as high angle grain boundaries (HAGBs), and those with misorientation angles between 2° and 15° were defined as low angle grain boundaries (LAGBs). The TiB whiskers in the maps were also represented. The measured textures were presented by {0001}, $\{11\bar{2}0\}$ and $\{10\bar{1}0\}$ pole figures, and the strong and weak texture components were represented by red and purple, respectively. The α_p and α_s grains were separated in the Ti60 matrix with HKL Channel 5 software.

3 Results and discussion

The recovery mechanism can be subdivided into two groups: by the continuous condensation of dislocations of deformed matrix crystal into new LAGBs and the transformation of LAGBs into HAGBs by lattice rotation, forming the new grains by continuous DRX. Moreover, by nucleation and grain growth with HAGB migration, the refined grains were formed by discontinuous DRX [13,14]. Upon recrystallization, new grains nucleated and grew up, resulting in the nonrandomness of grain orientation in polycrystalline aggregates, so as to form the new crystal texture, namely recrystallization texture [15]. The large plastic strain during hot compression usually leads to crystal bending and misorientation evolution, and the grains tend to realign into a preferred orientation after sufficient deformation, resulting in the development of a deformation texture [16], which has an important influence on the mechanical properties [17]. Commonly, a textured material usually exhibits anisotropic properties, to fully utilize the property anisotropy to the best advantage, it is necessary to manufacture a texture through hot compression for the particular strengthening purpose.

3.1 Flow stress−strain curves

The stress−strain curves of TiB_w/Ti60 composites at different strains are shown in Fig. 2. Much lower stress was required in two-phase isothermal forging than traditional forging methods [18]. It was clear that the curves showed obvious flow softening behavior at 1030 ℃ and strain rate of 10^{-2} s^{-1}. According to previous research [19], under the same compression parameters, the stress of TMC is always higher than that of Ti60 alloy due to the strengthening effect from the addition of ceramic reinforcements [20]. The steady state in the curves reflected the dynamic balance between hardening and softening effects, and the mechanism in stability domain was mainly associated to DRV, DRX and globularization of α lamellae [21], while the oscillation characteristics were attributed to DRX, flowing localization, unstable deformation and micro-cracking [22−24].

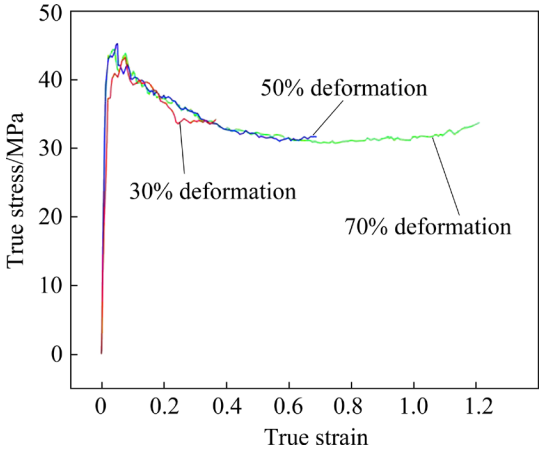

Fig. 2 Flow stress–strain curve of TiB_w/Ti60 composites deformed at 1030 ℃ and 1×10^{-2} s^{-1}

3.2 Microstructure evolution

Figure 3 shows the SEM images of TiB_w/Ti60 composites at different deformation degrees. In Fig. 3(a), the composites after RHP were fully compacted, showing a duplex microstructure composed by coarse equiaxed and lamellar α_p in Ti60 matrix, and the average grain size was ~63.54 μm. Lamellar α grains with good crack propagation resistance has superior creep and fatigue properties, while the equiaxed α grains with good deformation coordination has good plasticity and high cycle fatigue properties, contributing to the enhancement of crack propagation resistance [25,26]. Many studies have reported that the ductility of α+β titanium alloys can be improved by the presence of refined α grains with low aspect ratio [27,28], which can be obtained by the globularization of lamellar α grains, influenced by the DRX efficiency.

After RHP, TiB whiskers were in situ synthesized around Ti60 particles, forming a 3D

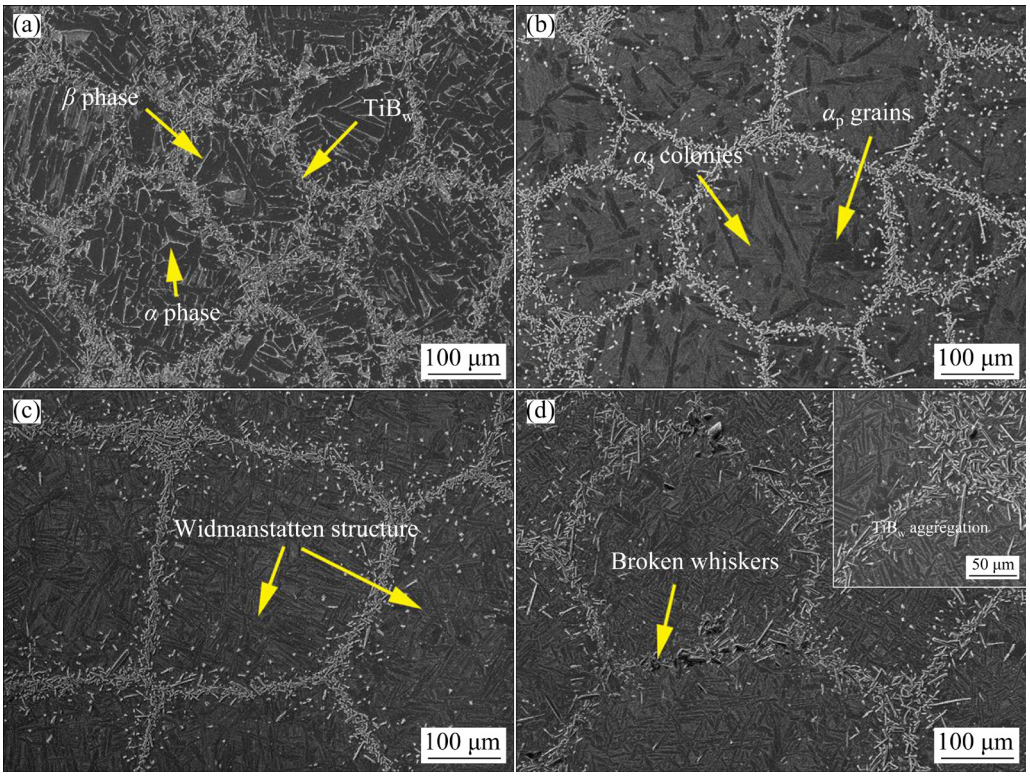

Fig. 3 SEM images of material at different deformation degrees: (a) Initial material; (b) 30% deformation; (c) 50% deformation; (d) 70% deformation

network structure with high local density, which had a negative influence on the plasticity and tensile properties due to poor matrix connectivity [29], and the average diameter of the network was ~161.2 μm. There was little residual β phase existed at room temperature, and thin β layers with width of ~1 μm were presented between the α lamellae. When strain increased, the initial coarse α_p grains gradually transformed into refined structure and surrounded by the α_s colonies converted from β phase (Fig. 3(b)). As deformation degree increased from 30% to 50%, no obvious TiB_w fracture phenomenon can be found in Fig. 3(c), the coarse α_p grains in the matrix were vanished, the volume fraction of α_p grains decreased form ~33.1% at 30% deformation degree to ~17.02%, and the average grain size increased form ~9.63 to ~20.21 μm, which was affected by the longer processing time and the coarse α_p grain in the network in Fig. 4(c). The morphology of TiB networks in the matrix changed with metal flow. With strain increasing, the average network diameter increased from ~225.9 to ~300.6 μm, resulting in a reduction in local volume fraction. As shown in Fig. 3(d), the coarse α_p grains were thoroughly refined at 70% deformation, the volume fraction of equiaxed α_p was ~33.47%, and the average grain size was ~13.62 μm. Many new refined DRX grains were randomly distributed around TiB whiskers. Some fractured TiB whiskers were found in the matrix [30], resulting in the flow stress softening and instability in flow stress–strain curve (Fig. 2). More nucleation sites were provided, and the DRX efficiency was thus increased. As mentioned above, the TiB network diameter extended to 357.2 μm with strain increasing, leading to the sparseness of local reinforcements, the ductility property was modified due to the fact that the connectivity of Ti60 matrix between TiBw network was generally improved. However, as shown in the upper right of Fig. 3(d), the network expansion inevitably led to the aggregation of reinforcements in some regions, which had a bad impact on the plasticity and tensile properties.

3.3 Electron backscattered diffraction analysis

Figure 4 exhibits the EBSD characterization of specimens at different deformation degrees. The orientation map of initial material in Fig. 4(a) showed coarse grains with sharp texture heterogeneities, which may decrease the fatigue

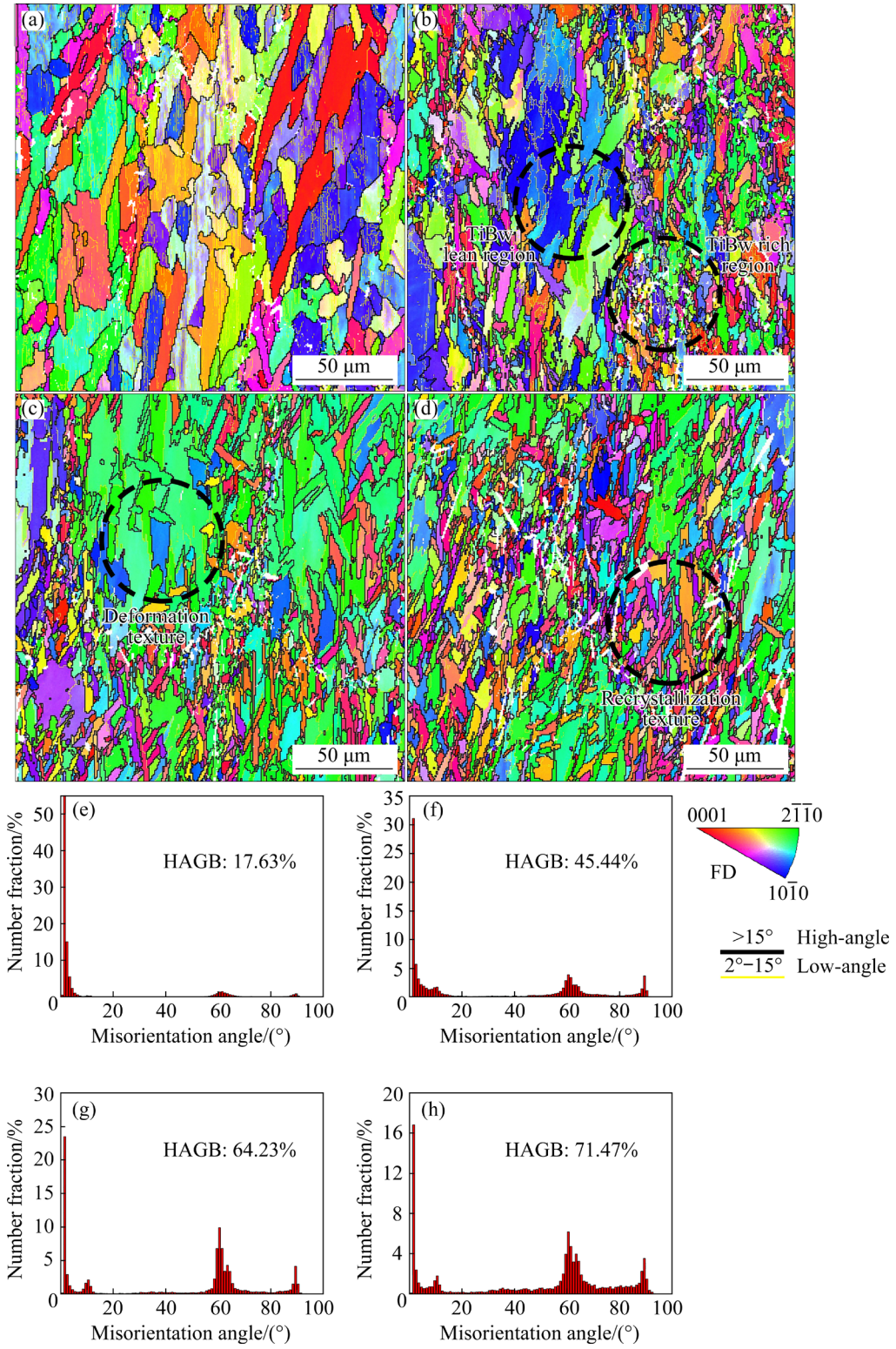

Fig. 4 Orientation distribution map of TiB_w/Ti60 composites of initial material (a), 30% deformation (b), 50% deformation (c) and 70% deformation (d), and misorientation angle distribution chart of initial material (e), 30% deformation (f), 50% deformation (g) and 70% deformation (h)

performances once it develops into sites of multiple initiating cracks [31]. During RHP process, the reinforcements had little influence on the matrix morphology in the map, the grains in TiBw lean and rich regions were homogeneous and similar.

During isothermal forging at 30% deformation degree, the matrix morphologies in both TiBw rich and lean regions were significantly changed. It can

be obviously seen in Fig. 4(b) that the α grains in the lower right corner were broken and surrounded by HAGBs, where the reinforcements were closely distributed. During hot compression, TiBw networks can impede the growth of the α_p lamellae by pinning effect and hindering dislocation movements, resulting in the inhomogeneous deformation between matrix and reinforcements [32]. Therefore, the regions near reinforcements contained high dislocation density and storage energy.

CHEN et al [33] found that the particle stimulated nucleation (PSN) mechanism plays a great role in the hot deformation of Ti−2Al−9.2Mo−2Fe−0.1B composites, with enough nucleation sites and pinning effect provided by TiB particles, the refined recrystallized microstructure can be achieved [34]. The nucleation and thin lamellar α_s globularization behavior occurred prior near the TiBw [10,35], which affected the crystallographic texture and thus material anisotropy properties. With strain increasing, the TiB particle stimulated nucleation mechanism became increasingly important in the recrystallization nucleation mechanism.

In contrast to the TiBw rich region, the volume fraction of LAGB in the middle of large reinforcements network in Figs. 4(b, c) was relatively high, which contained fewer TiB particles, suggesting the lower DRX efficiency. The coarse grains with *c*-axes perpendicular to the FD in Fig. 4(c) represented by blue and green were considered by the uniaxial hot compression, which indicated the typical deformation texture. Due to the dislocation accumulation under high deformation degree, some new grains with HAGB formed by the intragranular crystalline lattice rotation in the coarse α grains [36], suggesting the transformation from LAGB to HAGB in the TiBw lean region. At 70% deformation degree, more refined grains with various orientation distributions can be observed in the Ti60 matrix [37]. As shown in Figs. 4(e, f, g, h), with strain increasing, the HAGB fraction increased from 17.63% of initial material to 45.44% and 64.23%, and significantly increased to 71.47% at 70% deformation degree, which indicated that the increase of DRX efficiency. The new grains resulted from the gradual transformation of dislocation substructures produced by the strain hardening, leading to the increase of misorientation angle and the formation of HAGBs, the process is generally referred to be CDRX [38]. Some serrated boundaries of coarse α phase and necklace like grains can be spotted in the maps, which resulted from the grain boundaries migration, namely DDRX. So, the microstructure evolution mechanisms during forging process were composed of α lamellae globalization, grains growth, CDRX and DDRX.

After hot compression, the orientation distribution of α grains preferentially focused around the $\langle 11\bar{2}0\rangle$ axis. The misorientation angle distribution chart of α phase (Figs. 4(f, g, h)) indicated a relative high proportion around 10°, 60° and 90° between grains. For titanium alloys, the α_s colonies transformed from β phase had many variants [39], presenting obvious crystal orientation differences from the parent grains [40]. Around a TiB particle, the refined new grains were represented by different colors, suggesting various orientation distributions choices of new recrystallized grains. During phase transition of $\beta\rightarrow\alpha$, there were 12 different orientations inherited from β grains, which can be illustrated as $\{011\}_\beta//\{0001\}_\alpha$ and $\langle 111\rangle_\beta//\langle 1120\rangle_\alpha$ according to the Burgers orientation relationship (BOR), the formation of α_s colonies were characterized by several specific misorientations out of them. In the orientation map, there were many α grains with their *c*-axes in the radial directions, which mainly resulted from the activation of prismatic slip systems during hot compression, a gradual rotation of the lamellae toward the metal flow direction with strain increasing could promote the prismatic slip system and exhibited a typical deformation texture. At two-phase deformation, multiple slip systems were enhanced at high temperature, while the prismatic slip in HCP materials with lower *c*/*a* ratio was always easier to actuate than pyramidal and basal slip mode [41,42,43].

3.4 Texture evolution characterization

The crystallographic textures of initial material were presented by {0001}, $\{11\bar{2}0\}$ and $\{10\bar{1}0\}$ pole figures in Fig. 5. Obviously, there were many texture components with different orientation distributions in the map, which was in good agreement with the crystal orientation in Fig. 4(a) and conformed to the characteristics of powder metallurgy. The maximum intensity was ~12.36 times the random in {0001} pole figure.

It can be seen from Fig. 6 that after hot compression under 30% deformation degree, the characteristic of the main α_p texture components has changed greatly and did not overlap the original texture components, and the modified texture could be the result of plastic deformation and grain recrystallization. After forging process, the maximum texture intensity increased to ~20.05 times the random in {0001} pole figure and the strong texture components mainly concentrated around TD and ND [44], suggesting that the *c*-axes of α grains have gradually tilted away from the forging direction [45], and the textures in $\{11\bar{2}0\}$ and $\{10\bar{1}0\}$ pole figures were relatively weak. The α_s texture components in Fig. 6(c) had little overlap with pole figure in Fig. 6(a) [40], indicating that the α_s grains have limited influence while the α_p grains in Fig. 6(b) had a dominant position in the formation of texture at 30% deformation.

The pole figures at 50% deformation in Fig. 7(a) showed similar texture characteristics with Fig. 6(a). The maximum intensity slightly increased to 21.32 times the random in {0001} pole figure, thus the effect of strain increasing on the maximum

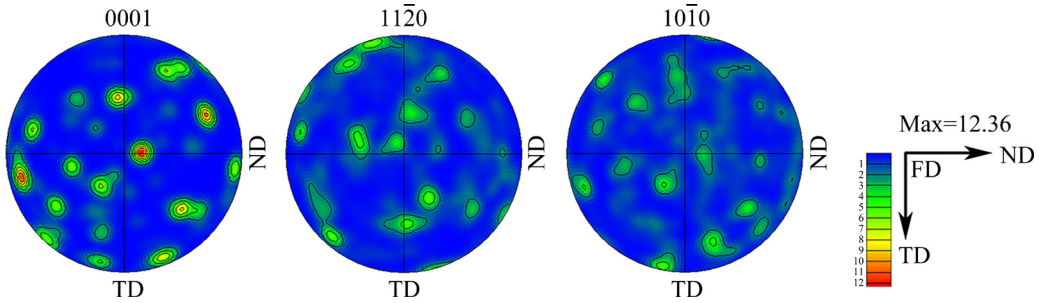

Fig. 5 Pole figures of α phase of as-received material

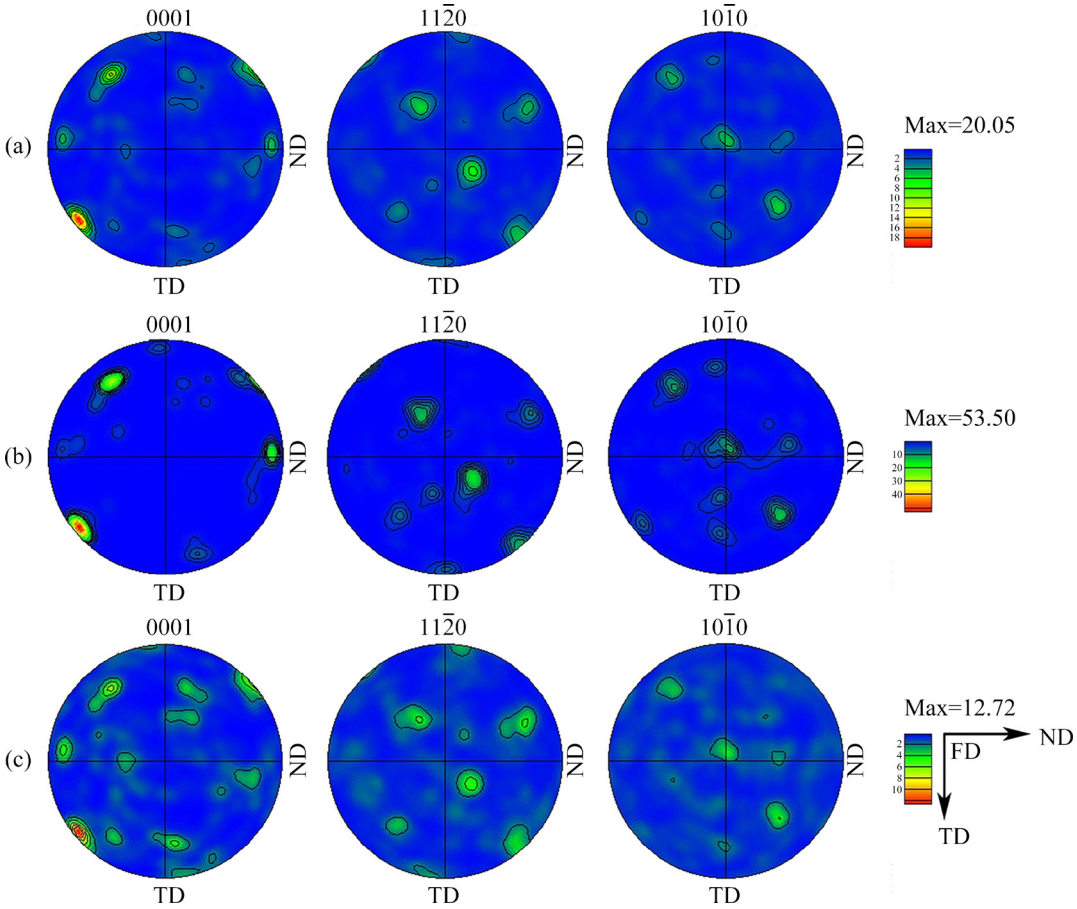

Fig. 6 Pole figures of α phase at 30% deformation (a), α_p phase at 30% deformation (b), and α_s phase at 30% deformation (c)

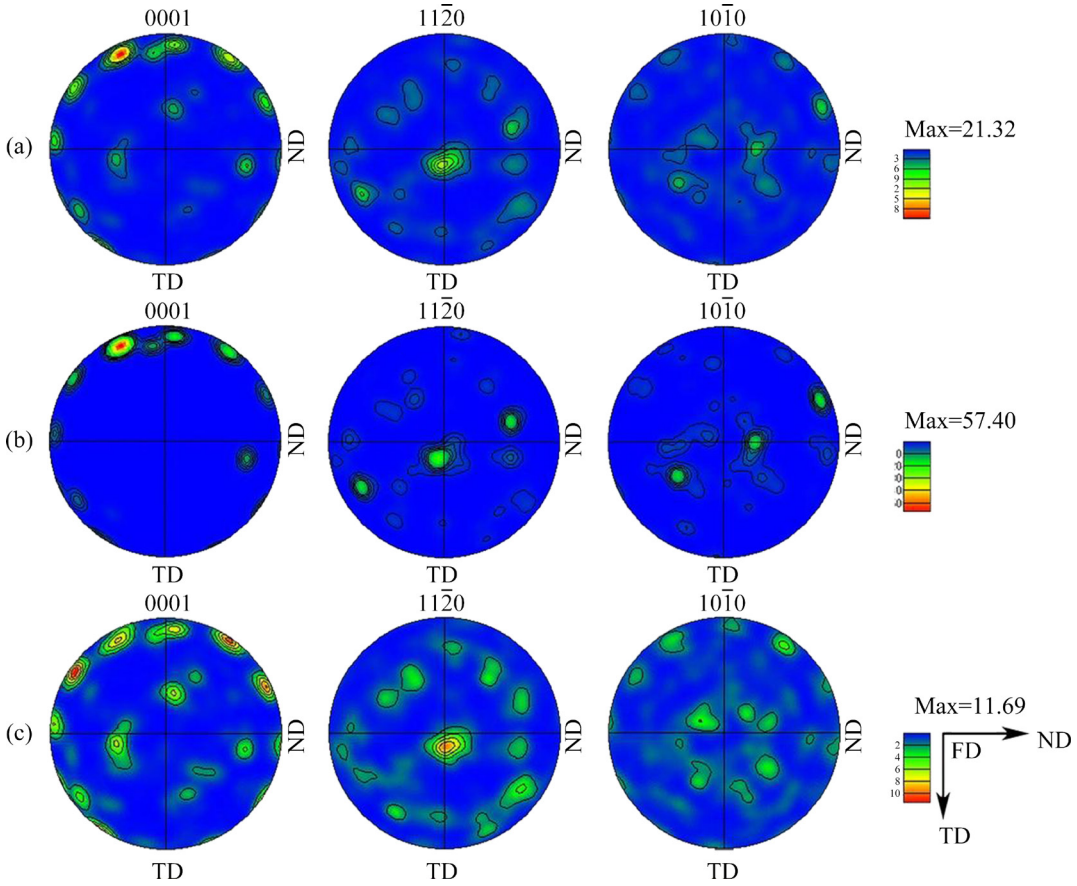

Fig. 7 Pole figures of α phase at 50% deformation (a), α_p phase at 50% deformation (b), and α_s phase at 50% deformation (c)

texture intensity seemed to be limited, and the deformation texture evolution was relatively stubborn. Due to uniaxial hot compression, the fiber texture of $\langle 11\bar{2}0\rangle$//FD with 13.75 times the random can be found in $\{11\bar{2}0\}$ pole figure [46], and multiple texture components of coarse α grains in $\{11\bar{2}0\}$ pole figure in Fig. 5 were eliminated and subdivided into α_s grains with various weak textures. In Fig. 7(a), the $\langle 11\bar{2}0\rangle$//FD fiber texture was stronger than that at 30% deformation, and the texture components were composed of the characterizations of both α_p grains and α_s grains in Figs. 7(b, c), suggesting that the influence of recrystallized α_s grains with multiple orientation choices was enhanced, which was consistent with the orientation map and misorientation angle distribution chart in Figs. 4(c, g).

The pole figure at 70% deformation is shown in Fig. 8. The maximum intensity was ~10.07 times the random in {0001} pole figure, which was weaker than other specimens [47]. With strain increasing, the fractured TiB whiskers have greatly promoted the PSN mechanism, the efficiency of recrystallization and globularization was enhanced, and much more refined recrystallized α_s grains with various orientation distributions were formed during phase transformation. As shown in Fig. 8(c), the texture components obviously overlapped with that in Fig. 8(a), suggesting that the texture of recrystallized grains became dominant at 70% deformation, while the effect form coarse α_p in Fig. 8(b) was relatively weak, leading to the decrease of the maximum texture intensity.

3.5 Tensile properties

After isothermal forging, the tensile specimens were machined from the geometric center of the forged material. The tensile tests were conducted at constant strain rate of 1×10^{-3} s^{-1} at room temperature and 600 ℃, respectively. High temperature oxidation resistant coating was used during 600 ℃ tensile test. The tensile properties are shown in Table 2, including yield strength, ultimate tensile strength and elongation. The stress−strain curves

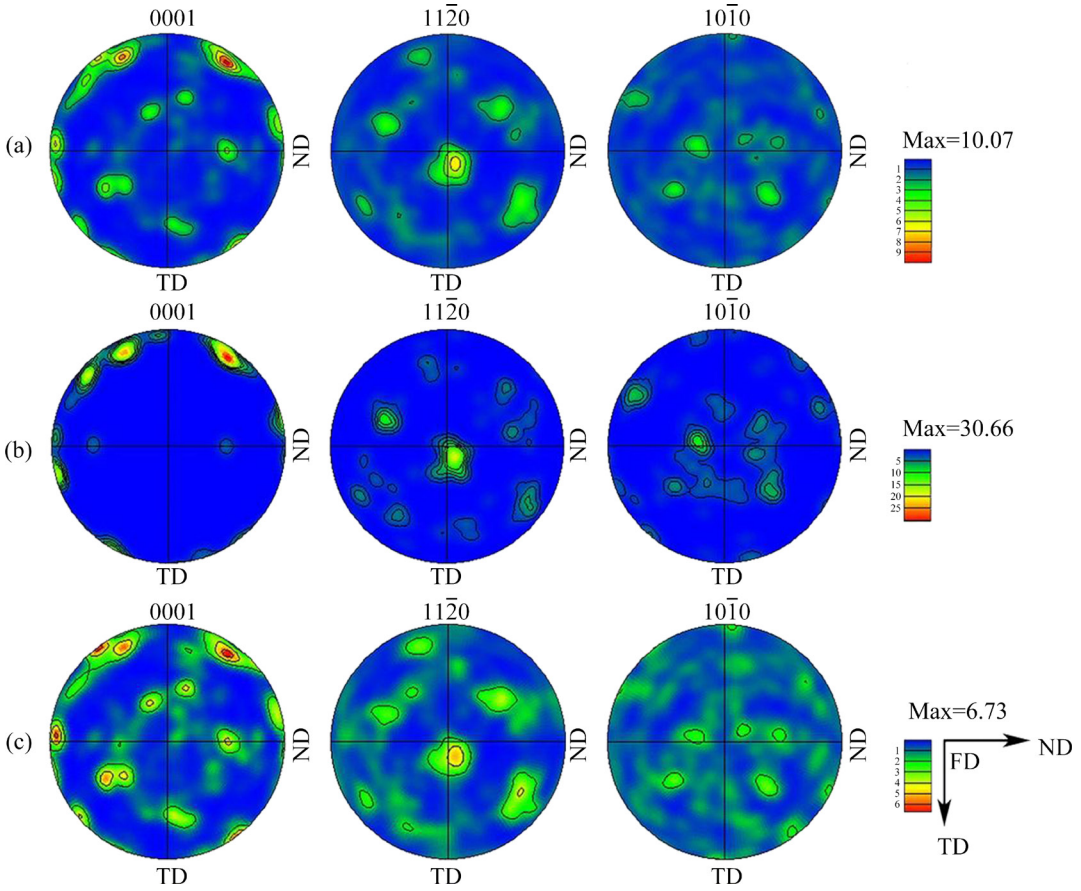

Fig. 8 Pole figure of α phase at 70% deformation (a), α_p phase at 70% deformation (b), and α_s phase at 70% deformation (c)

Table 2 Tensile properties of TiB_w/Ti60 composites under different deformations

Material	Tensile temperature/°C	Yield strength/MPa	Ultimate tensile strength/MPa	Elongation/%
Initial material	RT	1078.14	1127.39	1.45
	600	622.70	699.60	3.04
30% deformation	RT	1082.60	1237.35	2.51
	600	650.13	787.63	7.41
50% deformation	RT	1164.69	1246.20	3.55
	600	656.60	781.38	10.01
70% deformation	RT	1113.39	1171.63	2.08
	600	615.83	743.13	7.04

are shown in Fig. 9.

The TiB whiskers were synthesized through RHP process and distributed in the network boundaries, which can not only overcome the weakening effect of grain boundary at high temperatures, but also increase the strengthening effect of the grain boundary [48]. At high temperature tensile test, the thermally activated processes such as dislocation motion was promoted, and more slip systems were activated [49], which can minimize the dislocation pile-up and the local stress concentrations phenomenon [50]. By comparing the tensile properties and texture characterization, we can find that the hot compression contributed to the anisotropy of materials, and the tensile properties showed a positive changing tendency with maximum texture intensity. The maximum texture intensity increased

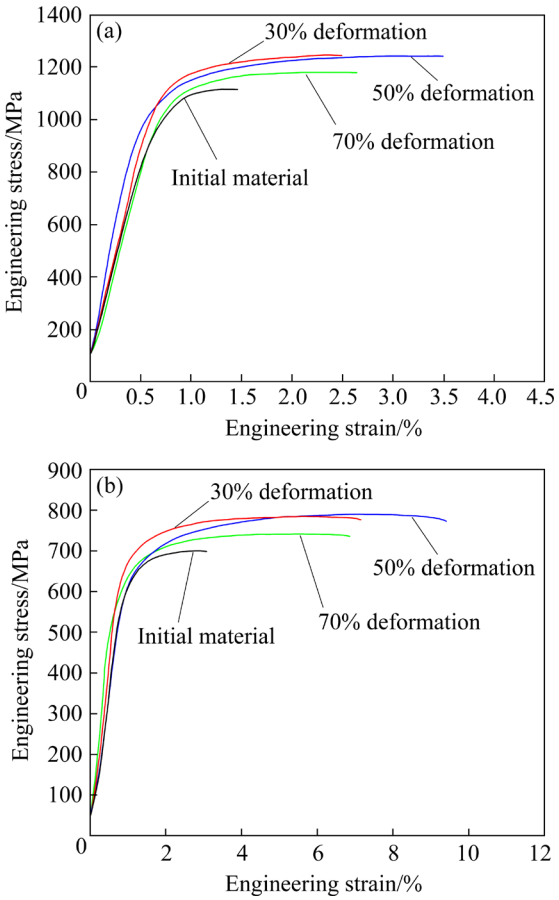

Fig. 9 Tensile engineering stress−strain curves of TiB_w/Ti60 composites at room temperature (a) and 600 ℃ (b)

with deformation degree increasing till 50% deformation degree, then decreased at 70% deformation according to the EBSD analysis, which is consistent with the tensile properties data in Table 2. Under different deformation degrees of 30%, 50% and 70%, the ultimate tensile strength increased by 9.76%, 10.56% and 3.91% at room temperature and 12.58%, 11.69% and 6.22% at 600 ℃, respectively. The specimen compressed at 50% deformation showed outstanding high temperature mechanical properties, the ultimate tensile strength and elongation increased to 781.38 MPa and 10.01% at 600 ℃. As deformation increased from 30% to 50%, the texture analysis results indicated the better anisotropy properties, and the expansion of TiB networks has promoted the connectivity between neighbouring matrix, leading to the higher ductility. The TiB networks showed less agglomeration phenomenon, so as to avoid the adverse effect on the mechanical properties.

Figure 10 shows the fracture surface micro-graphs of the 5.1vol.%TiB_w/Ti60 composites at different deformation degrees at RT and 600 ℃. It is confirmed that the hot compressed material can exhibit a better ductility property through grain refinement and the decrease of reinforcements local volume fractions. With strain increasing, the TiB whiskers gradually arranged along the direction of metal flow, which can join the adjacent Ti60 matrix particles and had a strengthening effect in the radial direction.

Many cleavage planes, rocky patterns and the TiB network structure with high local volume fractions can be observed in Fig. 10(a), and the initial material tested at RT exhibited cleavage feature. The material fractured preferentially along the interface of the TiB network, which can resist the crack propagation and enhance ductility properties. When tested at RT, the deformation coordination ability was insufficient, and the cracks preferentially propagated along a certain cleavage plane, leading to inferior ductility of the RHPed composites. The materials in Figs. 10(c, e, g) were hot compressed after sintering, and some dimples were observed in the fractograph, which can enhance the matrix plasticity. It can be seen that some TiB whiskers were fractured or pulled out of the matrix, during tensile tests the reinforcements can bear the load transmitted from surrounding matrix, showing strengthening effect on the tensile properties.

When tested at 600 ℃, as shown in Fig. 10(b), the fractograph of the initial material was similar to that at RT due to the high local density of TiB whiskers in the network, showing cleavage feature. After isothermal forging, the fracture morphology in Figs. 10(d, f, h) changed greatly in contrast to the as-received material. More dimples and matrix tearing ridges were presented, and dimples became larger and shallower with strain increasing, showing the superior fracture toughness. When tested at high temperature, more slip systems were activated and the material deformed more uniformly, which reduced the crack origination and improved the ductility. These characteristics suggested the predominant ductile fracture mechanism at high temperature. On the fracture surface, there were fewer fractured TiB whiskers than those tested at RT, some whiskers were pulled out of the matrix, so the strengthening effect form TiBw was relatively weak at 600 ℃.

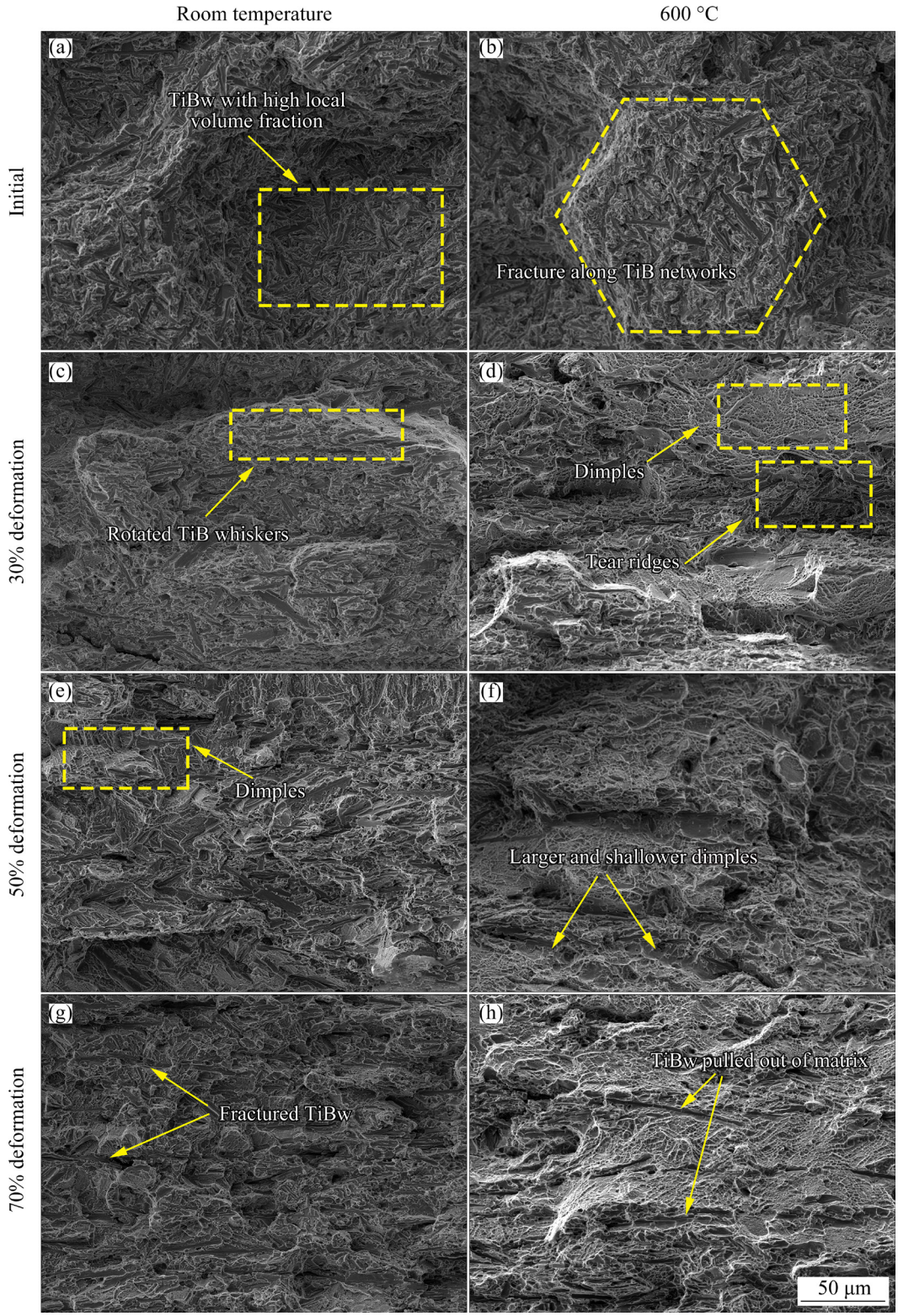

Fig. 10 SEM images showing fracture surfaces of TiB_w/Ti60 composites after tensile test at different temperatures

4 Conclusions

(1) Grain refinement of RHPed TiB_w/Ti60 composites was achieved through isothermal forging, and the grain refinement mechanism included CDRX and DDRX. With strain increasing, the fraction of HAGBs increased from 17.63% of initial material to 71.47% at 70% deformation.

(2) TiB whiskers can promote the DRX

efficiency, restrict grain growth and bear the load transmitted from Ti60 matrix. The local fraction of the reinforcements decreased with strain increasing, which enhanced the connectivity of Ti60 matrix between TiBw networks, so the plasticity was improved. At 70% deformation, the reinforcement aggregation phenomenon occurred in some regions, which had a bad influence on the ductility.

(3) The α_s phase gradually took the main position of the texture component characterizations with strain increasing. At 70% deformation, the texture of the refined recrystallized α grains took the lead, the maximum texture intensity kept increasing until 50% deformation, and decreased at 70% deformation.

(4) The tensile properties of initial material at both RT and 600 ℃ were improved after isothermal forging. The specimen compressed at 50% deformation showed the best tensile strength and elongation. The fracture mechanism of the initial materials showed cleavage fracture while the forged material had better plasticity and showed ductile fracture at 600 ℃ tensile test.

Acknowledgments

The authors are grateful for the financial support provided by the National Natural Science Foundation of China (Nos. 51701114, 11604204, 51805313), and the Youth Teacher Development Program of Shanghai Universities, China (No. ZZGCD15101).

References

[1] XU Jian-wei, ZENG Wei-dong, ZHOU Da-di, HE Sheng-tong, JIA Run-chen. Evolution of coordination between α and β phases for two-phase titanium alloy during hot working [J]. Transactions of Nonferrous Metals Society of China, 2021, 31: 3428−3438.

[2] ZHAO Er-tuan, SUN Shi-chen, YU Jin-rui, AN Yu-kun, CHEN Wen-zhen, CHEN Rui-run. Dynamic recrystallization and silicide precipitation behavior of titanium matrix composites under different strains [J]. Transactions of Nonferrous Metals Society of China, 2021, 31: 3416−3427.

[3] HUANG Guang-fa, HAN Yuan-fei, GUO Xiang-long, QIU Di, WANG Li-qiang, LU Wei-jie, ZHANG Di. Effects of extrusion ratio on microstructural evolution and mechanical behavior of in situ synthesized Ti−6Al−4V composites [J]. Materials Science and Engineering A, 2017, 688: 155−163.

[4] TJONG S C, MAI Y W. Processing-structure-property aspects of particulate- and whisker-reinforced titanium matrix composites [J]. Composites Science and Technology, 2008, 68: 583−601.

[5] MORSI K, PATEL V V. Processing and properties of titanium–titanium boride (TiBw) matrix composites — A review [J]. Journal of Materials Science, 2007, 42: 2037−2047.

[6] LIN Peng, FENG Ai-han, YUAN Shi-jian, LI Ge-ping, SHEN Jun. Microstructure and texture evolution of a near-α titanium alloy during hot deformation [J]. Materials Science and Engineering A, 2013, 563: 16−20.

[7] LUO jiao, LI Miao-quan. FE-based coupling simulation of Ti60 alloy in isothermal upsetting process [J]. Transactions of Nonferrous Metals Society of China, 2010, 20: 849−856.

[8] MAO Yong, LI Shi-qiong, ZHANG Jian-wei, PENG Ji-hua, ZOU Dun-xu, ZHONG Zeng-yong. Microstructure and tensile properties of orthorhombic Ti−Al−Nb−Ta alloys [J]. Intermetallics, 2000, 8: 659−662.

[9] WANJARA P, JAHAZI M, MONAJATI H, YUE S, IMMARIGEON J P. Hot working behavior of near-α alloy IMI834 [J]. Materials Science and Engineering A, 2005, 396: 50−60.

[10] LÜ Z D, ZHANG C J, FENG H, ZHANG S Z, HAN J C, JIA Y, DU Z X, CHEN Y Y. Effect of heat treatment on microstructure and tensile properties of 2 vol.% TiC_p/near-β Ti composite processed by isothermal multidirectional forging [J]. Materials Science and Engineering A, 2019, 761: 138064.

[11] WANG Wei, ZENG Wei-dong, XUE Chen, LIANG Xiao-bo, ZHANG Jian-wei. Microstructure control and mechanical properties from isothermal forging and heat treatment of Ti−22Al−25Nb (at.%) orthorhombic alloy [J]. Intermetallics, 2015, 56: 79−86.

[12] ZHAO Z B, WANG Q J, LIU J R, YANG R. Characterizations of microstructure and crystallographic orientation in a near-α titanium alloy billet [J]. Journal of Alloys and Compounds, 2017, 712: 179−184.

[13] AL-SAMMAN T, GOTTSTEIN G. Dynamic recrystallization during high temperature deformation of magnesium [J]. Materials Science and Engineering A, 2008, 490: 411−420.

[14] CHEN Yan, SHEN Ying-ju, LIU Xin, ZHONG Bi-neng. 3D object tracking via image sets and depth-based occlusion detection [J]. Signal Processing, 2015, 112: 146−153.

[15] GOURDET S, MONTHEILLET F. A model of continuous dynamic recrystallization [J]. Acta Materialia, 2003, 51: 2685−2699.

[16] WANG Y N, HUANG J C. Texture analysis in hexagonal materials [J]. Materials Chemistry and Physics, 2003, 81: 11−26.

[17] LÜTJERING G. Influence of processing on microstructure and mechanical properties of (α+β) titanium alloys [J]. Materials Science and Engineering A, 1998, 243: 32−45.

[18] MIURA H, KOBAYASHI M, AOBA T, AOYAMA H, BENJANARASUTH T. An approach for room-temperature multi-directional forging of pure titanium for strengthening [J]. Materials Science and Engineering A, 2018, 731: 603−608.

[19] PENG Wen-wen, ZENG Wei-dong, WANG Qing-jiang, ZHAO Qin-yang, YU Han-qing. Effect of processing parameters on hot deformation behavior and microstructural evolution during hot compression of as-cast Ti60 titanium

alloy [J]. Materials Science and Engineering A, 2014, 593: 16−23.

[20] HUANG L J, YANG F Y, HU H T, RONG X D, GENG L, WU L Z. TiB whiskers reinforced high temperature titanium Ti60 alloy composites with novel network microstructure [J]. Materials & Design, 2013, 51: 421−426.

[21] BAI X F, ZHAO Y Q, ZENG W D, JIA Z Q, ZHANG Y S. Characterization of hot deformation behavior of a biomedical titanium alloy TLM [J]. Materials Science and Engineering A, 2014, 598: 236−243.

[22] SESHACHARYULU T, MEDEIROS S C, FRAZIER W G, PRASAD Y V R K. Hot working of commercial Ti−6Al−4V with an equiaxed α–β microstructure: Materials modeling considerations [J]. Materials Science and Engineering A, 2000, 284: 184−194.

[23] LI A B, HUANG L J, MENG Q Y, GENG L, CUI X P. Hot working of Ti−6Al−3Mo−2Zr−0.3Si alloy with lamellar α+β starting structure using processing map [J]. Materials & Design, 2009, 30: 1625−1631.

[24] SEMIATIN S L, SEETHARAMAN V, WEISS I. Flow behavior and globularization kinetics during hot working of Ti−6Al−4V with a colony alpha microstructure [J]. Materials Science and Engineering A, 1999, 263: 257−271.

[25] SHI Zhi-feng, GUO Hong-zhen, ZHANG Jian-wei, YIN Jian-ning. Microstructure−fracture toughness relationships and toughening mechanism of TC21 titanium alloy with lamellar microstructure [J]. Transactions of Nonferrous Metals Society of China, 2018, 28: 2440−2448.

[26] JIA Run-chen, ZENG Wei-dong, HE Sheng-tong, GAO Xiong-xiong, XU Jian-wei. The analysis of fracture toughness and fracture mechanism of Ti60 alloy under different temperatures [J]. Journal of Alloys and Compounds, 2019, 810: 151899.

[27] ZHANG Z X, QU S J, FENG A H, HU X, SHEN J. Microstructural mechanisms during multidirectional isothermal forging of as-cast Ti−6Al−4V alloy with an initial lamellar microstructure [J]. Journal of Alloys and Compounds, 2019, 773: 277−287.

[28] ZHANG Z X, QU S J, FENG A H, SHEN J. Achieving grain refinement and enhanced mechanical properties in Ti−6Al−4V alloy produced by multidirectional isothermal forging [J]. Materials Science and Engineering A, 2017, 692: 127−138.

[29] HUANG L J, GENG L, PENG H X, ZHANG J. Room temperature tensile fracture characteristics of in situ TiBw/Ti6Al4V composites with a quasi-continuous network architecture [J]. Scripta Materialia, 2011, 64: 844−847.

[30] HUANG Li-guo, KONG Fan-tao, CHEN Yu-yong, XIAO Shu-long. Microstructure and tensile properties of Ti−6Al−4V−0.1B alloys of direct rolling in the near β phase region [J]. Materials Science and Engineering A, 2013, 560: 140−147.

[31] BIAVANT K L, POMMIER S, PRIOUL C. Local texture and fatigue crack initiation in a Ti−6Al−4V titanium alloy [J]. Fatigue Fract Eng Mater Struct, 2002, 25: 527−545.

[32] ROY S, SUWAS S. The influence of temperature and strain rate on the deformation response and microstructural evolution during hot compression of a titanium alloy Ti−6Al−4V−0.1B [J]. Journal of Alloys and Compounds, 2013, 548: 110−125.

[33] CHEN Rong, HUI Song-xiao, YE Wen-jun, YU Yang, MI Xu-jun, LEE D G, LEE Y T. High-temperature deformation behaviors of Ti−2Al−9.2Mo−2Fe alloy with boron [J]. Rare Metals, 2017, 7: 1−11.

[34] CHEN Rong, TAN Cheng-wen, YU Xiao-dong, HUI Song-xiao, YE Wen-jun, LEE Y T. Effect of TiB particles on the beta recrystallization behavior of the Ti−2Al−9.2Mo−2Fe−0.1B metastable beta titanium alloy [J]. Materials Characterization, 2019, 153: 24−33.

[35] HILL D, BANERJEE R, HUBER D, TILEY J, FRASER H L. Formation of equiaxed alpha in TiB reinforced Ti alloy composites [J]. Scripta Materialia, 2005, 52: 387−392.

[36] WANG B, HUANG L J, LIU B X, GENG L, HU H T. Effects of deformation conditions on the microstructure and substructure evolution of TiB_w/Ti60 composite with network structure [J]. Materials Science and Engineering A, 2015, 627: 316−325.

[37] WEISS I, SEMIATIN S L. Thermomechanical processing of beta titanium alloys—An overview [J]. Materials Science and Engineering A, 1998, 243: 46−65.

[38] ION S E, HUMPHREYS F J, WHITE S H. Dynamic recrystallisation and the development of microstructure during the high temperature deformation of magnesium [J]. Acta Metallurgica, 1982, 30: 1909−1919.

[39] GERMAIN L, GEY N, HUMBERT M. Reliability of reconstructed beta-orientation maps in titanium alloys [J]. Ultramicroscopy, 2007, 107: 1129−1135.

[40] GERMAIN L, GEY N, HUMBERT M, BOCHER P, JAHAZI M. Analysis of sharp microtexture heterogeneities in a bimodal IMI 834 billet [J]. Acta Materialia, 2005, 53: 3535−3543.

[41] FITZNER A, PRAKASH D G L, FONSECA J Q, THOMAS M, ZHANG Shu-yan, KELLEHER J, MANUEL P, PREUSS M. The effect of aluminium on twinning in binary alpha-titanium [J]. Acta Materialia, 2016, 103: 341−351.

[42] XU Shun, TOTH L S, SCHUMAN C, LECOMTE J S, BARNETT M R. Dislocation mediated variant selection for secondary twinning in compression of pure titanium [J]. Acta Materialia, 2017, 124: 59−70.

[43] LI N, ZHAO Z B, ZHU S X, ZHOU T Y, WANG Q J, SUN H, LIU Y H. Analysis of the active slip mode during compression of the near-α titanium alloy in the α+β phase-field: Insights from the results of electron backscattered diffraction [J]. Materials Letters, 2021, 288: 129363.

[44] LIU Y H, ZHAO Z B, ZHANG C B, WANG Q J, SUN H, LI N. Thermal and mechanical induced texture evolution of inertia friction welding in $\alpha + \beta$ titanium alloy [J]. Materials Letters, 2020, 277: 128329.

[45] ZHAO Z B, WANG Q J , LIU J R, YANG R. Effect of heat treatment on the crystallographic orientation evolution in a near-α titanium alloy Ti60 [J]. Acta Materialia, 2017, 131: 305−314.

[46] LIU Zheng, ZHAO Zi-bo, LIU Jian-rong, WANG Lei, YANG Guang, GONG Shui-li, WANG Qing-jiang, YANG Rui. Effect of α texture on the tensile deformation behavior of Ti−6Al−4V alloy produced via electron beam rapid manufacturing [J]. Materials Science and Engineering A,

2019, 742: 508−516.
[47] CHEN Yi, LI Jin-shan, TANG Bin, KOU Hong-chao, XUE Xiang-yi, CUI Yu-wen. Texture evolution and dynamic recrystallization in a beta titanium alloy during hot-rolling process [J]. Journal of Alloys and Compounds, 2015, 618: 146−152.
[48] HUANG L J, GENG L, PENG H X, KAVEENDRAN B. High temperature tensile properties of in situ TiBw/Ti6Al4V composites with a novel network reinforcement architecture [J]. Materials Science and Engineering A, 2012, 534: 688−692.
[49] JIA Wei-ju, ZENG Wei-dong, ZHOU Yi-gang, LIU Jian-rong, WANG Qing-jiang. High-temperature deformation behavior of Ti60 titanium alloy [J]. Materials Science and Engineering: A, 2011, 528: 4068−4074.
[50] DAVIES P, PEDERSON R, COLEMAN M, BIROSCA S. The hierarchy of microstructure parameters affecting the tensile ductility in centrifugally cast and forged Ti-834 alloy during high temperature exposure in air [J]. Acta Materialia, 2016, 117: 51−67.

等温锻造过程中变形量对 TiB_w/Ti60 复合材料显微组织和力学性能演变的影响

张芳洲，王 博，曹清华，张 利，张昊阳

上海工程技术大学 材料工程学院，上海 201600

摘 要：为了研究 TiB 晶须增强 Ti60 复合材料在热压缩过程中变形程度对微观结构和力学性能的影响，在 1030 ℃，应变速率为 1×10^{-2} s^{-1}，变形量为 30%、50%和 70%的条件下分别进行等温锻造。研究结果表明，随着应变的增加，大角度晶界(HAGBs)的比例在 70%变形量时显著上升到 71.47%。由于材料再结晶效率的提高，α_s 晶粒的织构成分逐渐成为主导织构成分。TiB 能够促进再结晶晶粒的形核并且阻碍晶粒长大。经过等温锻造，复合材料在室温和 600 ℃下的力学性能均有所提高，在 50%变形量时锻造试样具有最佳的拉伸强度和伸长率。在拉伸试验过程中 TiB 晶须承受周围基体传递的载荷，从而材料表现出强化效果。

关键词：钛基复合材料；等温锻造；动态再结晶；织构演变；力学性能

(Edited by Xiang-qun LI)